AGU PUBLICATIONS

JGR

Journal of Geophysical Research: Space Physics

RESEARCH ARTICLE
10.1002/2017JA024497

Key Points:
- We determined the influence of the main driving parameters on the altitude of the photoelectron boundary (PEB)
- We identified clear plasma and magnetic field characteristics of the PEB and discuss its nature with respect to the ionopause
- We show how the PEB dynamics modifies the tail cross section used for estimating the photoelectrons (and associated ions) escape rate

Correspondence to:
P. Garnier,
philippe.garnier@irap.omp.eu

Citation:
Garnier, P., Steckiewicz, M., Mazelle, C., Xu, S., Mitchell, D., Holmberg, M. K. G., … Jakosky, B. M. (2017). The Martian photoelectron boundary as seen by MAVEN. *Journal of Geophysical Research: Space Physics*, *122*, 10,472–10,485. https://doi.org/10.1002/2017JA024497

Received 21 JUN 2017
Accepted 2 SEP 2017
Accepted article online 11 SEP 2017
Published online 5 OCT 2017

The Martian Photoelectron Boundary as Seen by MAVEN

P. Garnier[1], M. Steckiewicz[1], C. Mazelle[1], S. Xu[2,3], D. Mitchell[2], M. K. G. Holmberg[1], J. S. Halekas[4], L. Andersson[5], D. A. Brain[5], J. E. P. Connerney[6], J. R. Espley[6], R. J. Lillis[2], J. G. Luhmann[2], J.-A. Sauvaud[1], and B. M. Jakosky[5]

[1]IRAP, Université de Toulouse, CNRS, UPS, CNES, Toulouse, France, [2]Space Sciences Laboratory, University of California, Berkeley, CA, USA, [3]Department of Climate and Space Sciences and Engineering, University of Michigan, Ann Arbor, MI, USA, [4]NASA Goddard Space Flight Center, Greenbelt, MD, USA, [5]Laboratory for Atmospheric and Space Physics, University of Colorado Boulder, Boulder, CO, USA, [6]Department of Physics and Astronomy, University of Iowa, Iowa City, IA, USA

Abstract Photoelectron peaks in the 20–30 eV energy range are commonly observed in the planetary atmospheres, produced by the intense photoionization from solar 30.4 nm photons. At Mars, these photoelectrons are known to escape the planet down its tail, making them tracers for the atmospheric escape. Furthermore, their presence or absence allow to define the so-called photoelectron boundary (PEB), which separates the photoelectron dominated ionosphere from the external environment. We provide here a detailed statistical analysis of the location and properties of the PEB based on the Mars Atmosphere and Volatile EvolutioN (MAVEN) electron and magnetic field data obtained from September 2014 to May 2016 (including 1696 PEB crossings). The PEB appears as mostly sensitive to the solar wind dynamic and crustal fields pressures. Its variable altitude thus leads to a variable wake cross section for escape (up to ∼ +50%), which is important for deriving escape rates. The PEB is not always sharp and is characterized on average by the following: a magnetic field topology typical for the end of magnetic pileup region above it, more field-aligned fluxes above than below, and a clear change of the altitude slopes of both electron fluxes and total density (that appears different from the ionopause). The PEB thus appears as a transition region between two plasma and fields configurations determined by the draping topology of the interplanetary magnetic field around Mars and much influenced by the crustal field sources below, whose dynamics also impacts the estimated escape rate of ionospheric plasma.

1. Introduction

Due to the absence of a strong intrinsic magnetic field, the thin Martian atmosphere directly interacts with the incident solar wind plasma. The ionized part of the atmosphere acts as a conductive obstacle, leading to a draping of the interplanetary magnetic field (IMF) around the planet and the formation of an induced magnetosphere.

Among the numerous processes at work in the Martian environment, the continuous ionization of the atmospheric neutrals by the extreme ultraviolet (EUV) photons from the Sun leads to the production of photoelectrons that play a key role in the heating balance of the atmosphere. In particular, the strong 30.4 nm Helium II line of the solar spectrum ionizes CO_2 and O atmospheric neutrals (Mantas & Hanson, 1979), which can be seen in the energy spectra of electrons at Mars or other bodies such as Titan, Venus, and Earth (Coates et al., 2011) as two peaks between 21 and 24 eV and at 27 eV.

The Mars Global Surveyor (MGS) MAG/ER instrument revealed a strong change of the electron spectra at the external limit of the ionosphere (Mitchell et al., 2000, 2001), with, in particular, a photoelectron boundary (PEB) or ionopause defined by the disappearing of photoelectron features in the 20–50 eV energy range as well as near 500 eV (i.e., Auger electrons) and a change of the slope below 100 eV. These authors already mentioned the possible influence of crustal fields on the altitude of the observed boundary. The finer-energy resolution ($\delta m/m$ = 7% compared to 25% for MGS) of the Mars Express ASPERA ELS instrument (Barabash et al., 2006) then allowed the two photoelectron peaks in the 20–30 eV range to be resolved and the plasma boundaries at Mars to be investigated in more details (Lundin et al., 2004). Frahm et al. (2006, 2010) also revealed that a portion of the photoelectrons actually escape down to the tail behind the planet along draped open field lines, thus providing an insight into the escape rate of ionospheric plasma, assuming overall neutrality

of the plasma (see also Liemohn et al., 2006, who modeled the magnetic connectivity for Martian photoelectrons from the dayside to the wake). Such photoelectrons are known to be common in planetary atmospheres, such as at Titan, Venus, or Earth (see Coates et al., 2011; Tsang et al., 2015; Wellbrock et al., 2012).

Nevertheless, the definition of the Martian plasma boundaries still raises debates regarding their nature depending on the parameters observed (composition, density gradient, magnetic topology, pressure balance, etc). In particular, the PEB (determined from the disappearance of CO_2 20–30 eV photoelectrons) and the ionopause (determined from electron density gradients or density levels) were often observed at the same locations, but not systematically. Han et al. (2014) used Mars Express MARSIS and ASPERA data from 2005 to 2013 to obtain a median altitude of the ionopause at about 450 km, while the PEB altitude was located 200 km above this. However, no detailed analysis of the boundary characteristics or drivers of influence was performed, except for the solar zenith angle (SZA) variability.

The Mars Atmosphere and Volatile Evolution (MAVEN) mission, designed to study the structure, composition, and variability of the upper atmosphere and ionosphere of Mars, reached Mars in September 2014 (Jakosky et al., 2015). The complete plasma and magnetic field instruments package, combined with the spacecraft's elliptical orbits reaching low altitudes (down to 110 km during deep-dip campaigns), allows us to analyze the Martian plasma environment and the ionosphere in more detail. Recently, Sakai et al. (2015) used a two-stream electron transport code to interpret the photoelectron and Auger electron observations of the MAVEN Solar Wind Electron Analyzer (SWEA) instrument (Mitchell et al., 2016). They showed, in particular, how the solar irradiance, external electron fluxes, and ionospheric thermal electron density control the photoelectron spectrum. Xu, Mitchell, et al. (2016) also showed the presence of photoelectrons in the nightside ionosphere, very likely due to transport along closed crustal magnetic field loops that cross the terminator and extend far into the deep nightside.

In this paper, we use MAVEN electron and magnetic field data to analyze the photoelectron boundary in detail. After a description of the instruments and data set used for the study (section 2), we will discuss the geographical distribution of the boundary crossings (section 3) and the parameters driving its variability (section 4). We will then discuss the influence of the PEB on photoelectron escape (section 5) before we characterize in detail the boundary itself and its near environment through several parameters (section 6) and end with conclusions (section 7).

2. Description of the Data Set

2.1. Description of the Instruments

The MAVEN Solar Wind Electron Analyzer (SWEA) instrument is a symmetric, hemispheric, electrostatic analyzer with deflectors (Mitchell et al., 2016). It is designed to measure the energy and angular distributions of electrons within an energy range of 3 to 4,600 eV, with an energy resolution of $\delta E/E = 17\%$ and maximum time resolution of 2 s (depending on the mode used). MAVEN is not a spinning spacecraft but a three-axis stabilized spacecraft, so that SWEA uses deflectors to sweep the field of view (of $360° \times 7°$ for the hemispheres) to reach a maximum field of view of $360° \times 120°$ (i.e., 87% of the sky).

Moreover, we will use in this study the magnetic field measurements provided by the MAG instrument. It consists of two independent triaxial fluxgate magnetometer sensors, which measure the ambient vector magnetic field at an intrinsic sample rate of 32 vector samples per second over a wide dynamic range (until 65,536 nT per axis) with a maximum resolution of 0.008 nT and an accuracy of better than 0.05% (Connerney et al., 2015).

2.2. The Photoelectron Boundary Data Set

Figure 1 shows an example of a periapsis passage of MAVEN in February 2015, with the SWEA energy spectrograms and orbital parameters. The (X, Y, Z) coordinates are given in the MSO frame, where X points toward the Sun, Y points approximately opposite to Mars orbital angular velocity, and Z completes the right-handed set. The spacecraft was thus, at first, located in the dayside southern magnetosheath (a shocked and heated spectrum typical for the magnetosheath at 02:12 is shown in Figure 1e), with a draping and strong gradient of the magnetic field (not shown) from 02:13 UT, until a large drop of the energetic electron fluxes at about 02:18 UT and the appearance of the strong photoelectron peak at 20–30 eV. The spacecraft thus enters the ionosphere (a typical spectrum at 02:24 UT is shown in Figure 1d) and reaches the terminator region near 02:30 UT. The photoelectron double peak (between 21 and 24 and at 27 eV) appears as a single peak due to the energy

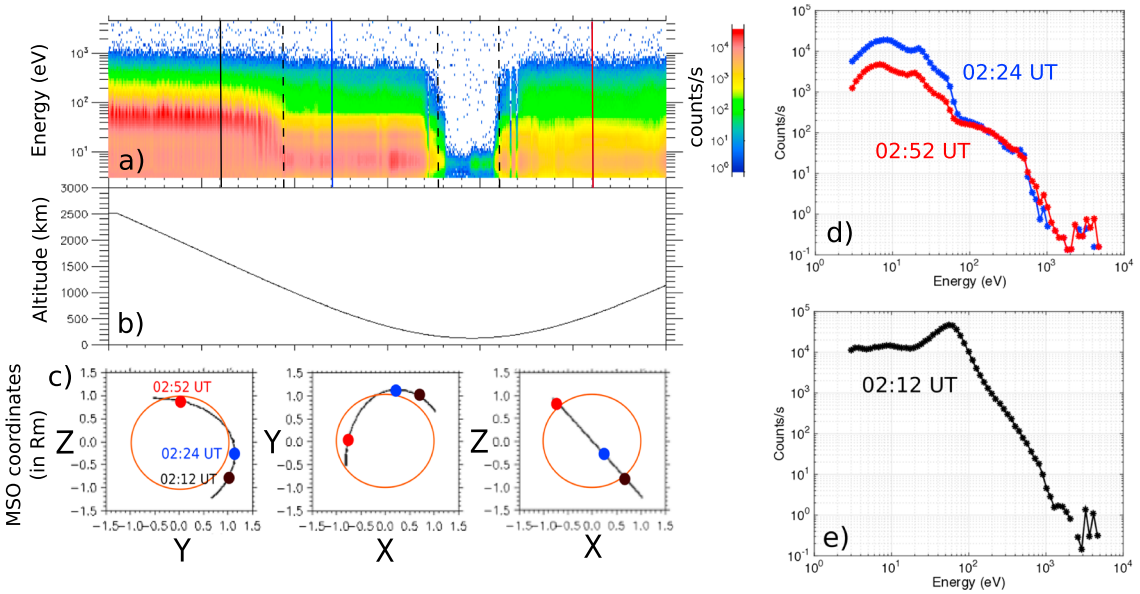

Figure 1. Case study on 12 February 2015. (a) MAVEN SWEA electron energy spectrogram with the color bar giving the omnidirectional counts per second. The dashed black lines show the crossings of the 20–30 eV photoelectron line, while the black/blue/red solid lines correspond to the times of the individual energy spectra given in Figures 1d and 1e. (b) Altitude of the spacecraft. (c) (*X*,*Y*,*Z*) coordinates of the spacecraft in the MSO frame, where *X* points toward the Sun, *Y* points opposite to Mars orbital angular velocity, and *Z* completes the right-handed set. (d) SWEA electron energy spectra typical for the dense ionosphere (blue) or escaping photoelectrons (red) in the tail. (e) Typical magnetosheath SWEA electron spectrum.

resolution of the instrument (except during negative charging events where the line splits into two different lines). Please note that the broad energy peak around 60 eV seen in the magnetosheath spectrum at 02.12 is not associated with photoelectrons but is a typical feature of the heated solar wind particles. A suprathermal electron depletion is then observed around periapsis (02:36 UT to 02:42 UT), since the spacecraft is located in the low-altitude nightside ionosphere where the absorption by CO_2 neutrals depletes almost all suprathermal electrons while the major ionization process—that is, photoionization—is stopped (see Steckiewicz et al., 2015, 2017, for further details). The CO_2 photoelectron line at 20–30 eV thus disappears as the spacecraft moves through the depletion region and reappears at 02:42 UT where it appears again until the end of the period shown, while the spacecraft is located behind the terminator in the tail: these photoelectrons are thus escaping the planet, with a line more diffuse than in the deep ionosphere (see also Coates et al., 2015 and Tsang et al., 2015 for similar observations at Venus).

The three dashed lines in Figure 1 show where the photoelectron line appears or disappears during this case study, corresponding to either the PEB (near 02:19) or to the edges of the electron depletions (at 02:35 and 02:42). We analyzed by hand the SWEA spectrograms and energy spectra from September 2014 to the end of May 2016, and identified 3,022 timings where the photoelectron line appeared or disappeared. An automatic (peak) detection algorithm was used at first, which worked well for large photoelectron peaks below the PEB, but it could hardly detect precisely the faint peaks that often appear close to the PEB (all the more that intermittent photoelectron line crossings are considered as PEB crossings). More than half of the automatic crossings timings had to be corrected by a few minutes, so that we chose to define the crossings manually for a better precision. The automatic algorithm will be, however, discussed in a future paper on a statistical analysis of the ionospheric photoelectrons.

Among these 3,022 crossings, 1,696 correspond unambiguously to dayside PEB crossings, the rest corresponding to edges of electron depletions in the nightside (all suprathermal electron fluxes drop, including the photoelectron fluxes), edges of detached escaping photoelectrons in the wake, or ambiguous crossings below the extreme ultraviolet terminator (here defined by a minimum altitude of 140 km). We thus defined as PEB crossings only the photoelectron line crossings taking place on the dayside ($X > 0$) at altitudes above the EUV terminator (see also Figure 3 later). The timings of the crossings are defined with a precision of ~30 s and define the last (or first) time interval where the photoelectron peak at 20–30 eV is unambiguously observed. The crossings on the dayside are easier to determine, whereas the times where the photoelectron line appears

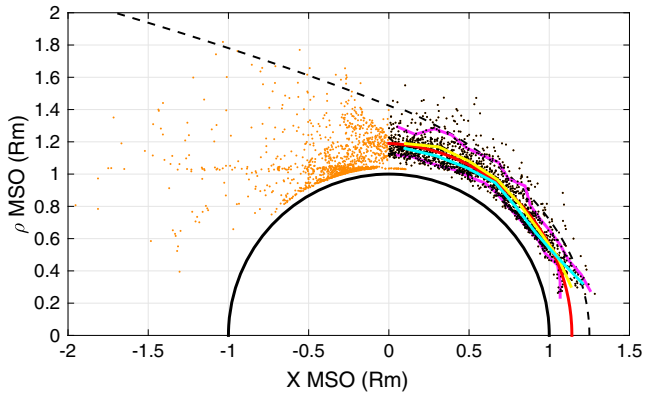

Figure 2. Geographical distribution of the photoelectron line crossings—PEB crossings in black dots, other crossings in orange—in cylindrical coordinates (in the plane (X, ρ) with $\rho = \sqrt{Y^2 + Z^2}$ the distance to the X axis; $1R_M \approx 3{,}390$ km average Martian radius). The dashed black line provides the average location of the magnetic pileup boundary fit by Trotignon et al. (2006). The cyan and yellow solid lines show, respectively, the northern and southern median location of the PEB (for 10° solar zenith angle bins), while the red curve shows the best conic fit for the dayside PEB crossings (see text for more details). The magenta lines show the limits including 80% of the PEB crossings.

or disappears in the tail or nightside ionosphere are much more difficult to define precisely due to the more diffuse structure of the peak. A number of small nightside electron depletions are also not included in the total data set, as well as temporary crossings in the tail where the line is more intermittent, due to the strong plasma dynamics (mixing of several populations, accelerated particles, etc.) occurring in this region. As will be discussed later, the PEB, even on the dayside, can barely be defined with a high precision due to the interpretation of the spectra which often show faint peaks before showing strong unambiguous peaks. The PEB appears as a transition region where the photoelectron flux gradually decreases, more or less sharp depending on the conditions (see section 6).

3. Geographical Distribution of the PEB

3.1. Overall Distribution

Figure 2 shows the geographical distribution of the 3,022 photoelectron line crossings (1,696 PEB crossings) in MSO cylindrical coordinates. No crossing was found at low SZA values (i.e., below 10° SZA) due to the orbital characteristics of MAVEN with few passages at the appropriate altitudes below 10° SZA. The PEB crossings cover a SZA range from ~10° SZA to ~90° SZA. Almost all crossings were confined within the average magnetic pileup boundary fit by Trotignon et al. (2006), determined from the Phobos 2 and Mars Global Surveyor data sets, in a shell of about 0.15–0.2 R_M ($1R_M \approx 3{,}390$ km average Martian radius).

The altitude of the dayside PEB crossings strongly varies between 186 and 1,931 km, with median and average altitudes, respectively, at 528 and 573 km (without including any SZA dependency). This is in close agreement with the Mars Express results by Han et al. (2014), who obtained an average altitude between 553 and 633 km depending on the SZA regime. The suprathermal electrons, thanks to their large mean free path and cross field diffusion in the absence of open draped lines, thus transport vertically to high altitudes (compared to the suprathermal electron exobase at ~145–165 km, see Xu, Liemohn, Bougher, et al., 2016), and are stopped on average before the other plasma boundaries such as the ion composition boundary (ICB), magnetic-pileup boundary (MPB), or pressure β^* boundary (Matsunaga et al., 2015; Xu, Liemohn, Dong, et al., 2016). We can mention that the MPB (named like this by numerous authors, see initially Nagy et al., 2004 or Bertucci et al., 2004) is also often called induced magnetosphere boundary (cf. Brain et al., 2017 or Dubinin et al., 2006), after it was even called at first planetopause (Riedler et al., 1989) or magnetopause (Rosenbauer et al., 1989).

Except near noon (see below for further details), the southern median location (yellow line) of the PEB is always at higher altitudes than the northern one (cyan line), in particular, close to the terminator where the difference reaches ~200 km, presumably due to the influence of the strong crustal magnetic fields of the southern hemisphere, which will be further discussed in section 4. The thickness of the altitude shell (defined by, for example, 80% of the PEB crossings inside the shell, magenta lines) increases from about 230 km at low SZA values until ~800 km near the terminator, as expected from the topology of the draping of the IMF around the planet that is more variable at terminator than at noon (as seen for the MPB location, see Trotignon et al., 2006).

A conic fitting of the dayside PEB crossings—defined by $r = \frac{L}{1+e*\cos(\theta)}$ with r and θ polar coordinates with origin at X_0 referenced to the X axis, and L and e the semilatus rectum and eccentricity; see Edberg et al. (2008) for further details—provides the following results: $(X_0, L, e) = (0R_M, 1.19R_M, 0.0047)$, which is almost identical to the Mars Express (Han et al., 2014) derived results values ($0.01\ R_M$, $1.19R_M$, 0.005). The average location of the PEB is thus very close to a circle (red line) centered on the planet center, as can be expected for the innermost plasma boundary. The closer the boundary, the lower the eccentricity: the MPB and bow shock best conic fits respectively correspond to eccentricities of 0.92/0.90 (Edberg et al., 2008)/(Vignes et al., 2002) and 1.05/1.03 (Edberg et al., 2008)/(Trotignon et al., 2006; Vignes et al., 2002).

3.2. Solar Zenith Angle and Local Time Variability

Figures 3 and 4 show the altitude, solar zenith angle (SZA), and local time (LT) variability of the 3,022 photoelectron line crossings determined during the two first years of the MAVEN mission. The photoelectron line

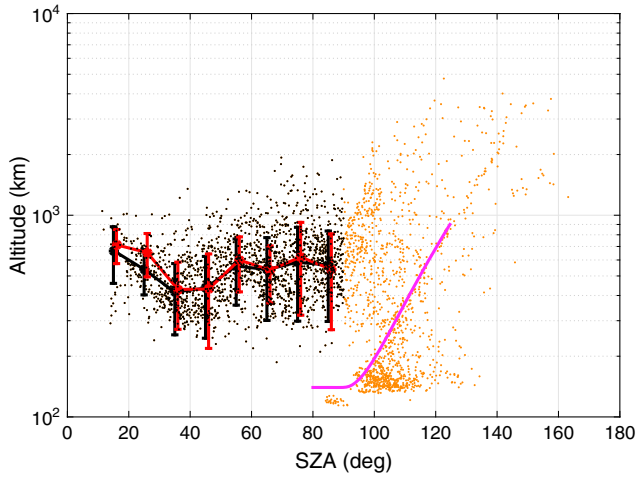

Figure 3. Altitude of the photoelectron line crossings—PEB crossings in black dots, other crossings in orange—as a function of the solar zenith angle (SZA). The magenta solid line provides the extreme ultraviolet terminator limit (where most photons are absorbed) corresponding to a lower limit at 140 km altitude. The black solid line shows the median altitude for SZA bins of 20° with the standard deviation, while the red solid line shows the median and standard deviation altitude for SZA values recalculated after including the aberration angle induced by the solar wind and after rotating the initial MSO frame into the MSE frame (see text for further details).

crossings beyond 90° SZA or below the extreme ultraviolet terminator (for a lower limit altitude of 140 km) are not a priori considered as real PEB crossings, even if some of them could be included as well. Until 30° SZA, the median altitude of the PEB crossings decreases at first, and then increases until a constant value below 600 km from 55° SZA. The increase of the PEB altitude is expected toward the terminator, since the draped field lines induce an increase of the MPB altitude with SZA, but larger altitudes closer to noon are unexpected. Moreover, the median local time variability in the MSO frame shows an unexpected and significant asymmetry, with a minimum altitude displaced with respect to noon, whereas the draping topology can be considered as symmetric. Where do these unexpected features come from? One can mention that a separation of the data sets into northern hemisphere and southern hemisphere observations (not shown) reveals higher altitudes in the south than in the north (presumably due to an enhanced crustal field pressure, see next section), except again near noon (in both SZA and LT) where the trend is reversed.

Since the draping of the IMF around Mars—and the Martian interaction with the solar wind in general—is known to depend significantly on the clock angle of the IMF (Carlsson et al., 2008), the PEB is expected to depend on it as well. Moreover, the solar wind velocity compared to the orbital velocity of the planet around the Sun induces a small but nonnegligible aberration angle (of a few degrees). We thus recalculated the SZA and LT values in the MSE frame that also includes a 4° aberration angle, based on the solar wind velocity and magnetic field parameters provided by the MAVEN SWIA and MAG instruments at each orbit (Halekas et al., 2017). The resulting new LT median variability (red line) shows a much more symmetric behavior: the PEB is thus strongly organized by the solar wind magnetic field direction, whose variability induces a continuous rotation of the draping around the *X* axis and thus a reorganization in terms of local time. One can also mention that the latitudinal variability of the PEB (not shown) is much more homogeneous in this modified MSE frame than in the MSO frame.

However, the SZA variability is obviously only slightly influenced by a small aberration angle, so that the unexpected high-altitude PEB crossings near noon need another explanation. Figure 5 shows the SZA variability of the crustal magnetic field (at a constant altitude of 400 km; Morschhauser et al., 2014) and solar wind dynamic pressure at the times of the photoelectron line crossings. A clear bias thus appears in our data set close to noon, with low solar wind dynamic pressures and high crustal magnetic field values. As will be detailed in the next section, both the solar wind and crustal magnetic field pressures are important drivers for the PEB location, since the pressure will push from above (for the solar wind) or below (for crustal fields) the draping magnetic field topology and modify the location where the upward moving photoelectrons will encounter the draped open field lines to get eventually convected toward the tail. A combination of (relative) low solar wind dynamic pressure and strong crustal field pressure will thus induce high altitudes for the PEB as observed in our data set.

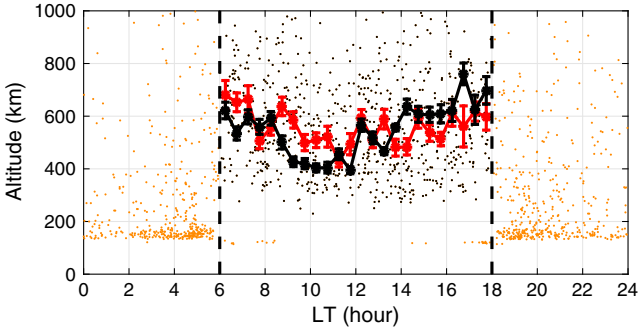

Figure 4. Altitude of the photoelectron line crossings—PEB crossings in black dots, other crossings in orange—as a function of the local time (LT). The dashed lines show the terminator, while the solid lines show the median altitude for LT bins of 0.5 h in the initial MSO frame (black line) and in the MSE frame (red line) that also includes the aberration angle induced by the solar wind (see text for further details).

4. The Parameters of Influence for the PEB: Solar Wind Dynamic and Crustal Magnetic Fields Pressures

The conic fitting of the dayside PEB crossings leads to a nearly circular shape of the boundary. Nonetheless, from now on we will only use the extrapolated terminator distance (i.e., $r_i(1 + e \times \cos(\theta_i))$ or altitude of the PEB to remove the average SZA variability of the PEB altitude, following previous works on the MPB or bow shock (Crider et al., 2003; Edberg et al., 2008).

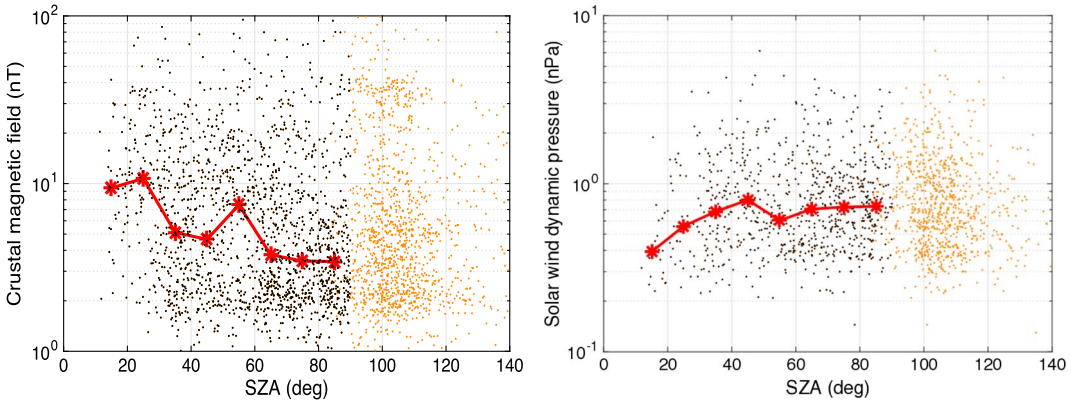

Figure 5. Demonstration of the SZA sampling bias for the PEB crossings data set: SZA variability of (left) the crustal magnetic field and (right) solar wind dynamic pressure at the times of the photoelectron line crossings, with PEB crossings in black dots, other crossings in orange, and the median values in solid red line. The crustal magnetic field is given by the Morschhauser et al. (2014) model at a constant altitude of 400 km.

4.1. The Influence of the Crustal Magnetic Field and Solar Wind Dynamic Pressure

The influence of the crustal field intensity on the PEB altitude is shown in Figure 6, where the estimated terminator altitude is given as a function of the longitude in the geographical IAU frame. This frame is fixed to the planet, with the strongest crustal fields region in the southern hemisphere at longitudes between 120 and 240°. The data set is separated into longitude and latitude regions to separate the strong and weak crustal field regimes, as defined by Edberg et al. (2008), with the strong fields in the following ranges: longitude from 0 to 120° and latitude from −45 to 45°, longitude from 120 to 240° and latitude from −90 to 0°, and longitude from 240 to 360° and latitude from −45 to 45°.

The median altitudes are systematically higher for the strong crustal field regime than for the low crustal field regime, by about 100 km or even 140 km in 120 to 240° longitude region where the strongest crustal fields are located. Edberg et al. (2008) obtained very similar results for the influence of crustal fields on the MPB and bow shock position, with the largest influence in the middle longitude range as well, with an altitude variation, that is, all the larger than the boundary is far: up to ∼400 km and ∼0.48 R_M for, respectively, the MPB and bow shock. One can also note that an IAU mapping of the PEB terminator altitude from our data set gives a good correlation with the location of crustal field sources.

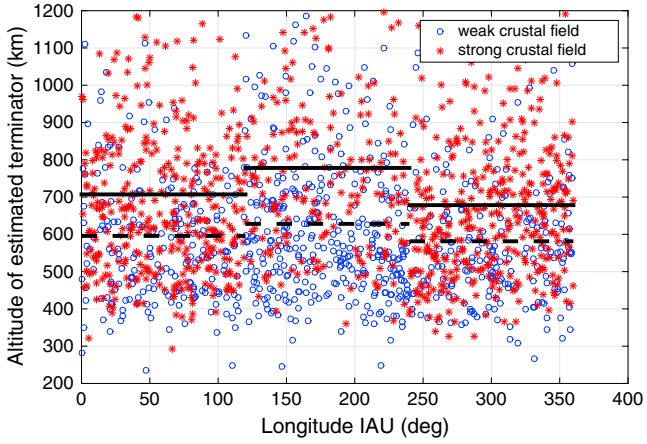

Figure 6. Estimated terminator altitude of the PEB crossings as a function of the longitude in the geographical IAU frame. The data set is separated into longitude and latitude regions to separate the strong and weak crustal field regimes, as defined by Edberg et al. (2008) (see text for more details). The blue circles and red stars correspond to PEB crossings in weak and strong crustal field regions, while the solid and dashed lines correspond to median altitudes for, respectively, strong and weak crustal field conditions in each of the three longitude bins.

The combined influence of the solar wind dynamic pressure and crustal magnetic field is shown in Figure 7. Despite a strong dispersion and a limited number of PEB crossings at high solar wind dynamic pressure values, the PEB terminator altitude clearly decreases while the solar wind dynamic pressure increases, with a median altitude decreasing from ∼700 km to ∼500 km. The separation between weak and strong crustal field crossings is also clear, with few high-altitude crossings located above weak crustal field regions. Power law fits were performed of the form $d_{\mathrm{term_{PEB}}} = a \times P_{\mathrm{SW}}^{b}$ with $d_{\mathrm{term_{PEB}}}$ terminator distance of the PEB in R_M and P_{SW} the solar wind dynamic pressure, for all crossings together (magenta line in the figure) or by separating weak (blue line) and strong (red line) crustal field crossings. The results are the following: $(a, b) \approx (3.60, -0.034)$ for all crossings; $(3.59, -0.034)$ for crossings above weak crustal fields; and $(3.61, -0.039)$ for crossings above weak crustal fields. The influence of the solar wind dynamic pressure is thus on average 40% smaller than on the MPB, for which the power law index value was estimated at about −0.055 (Crider et al., 2003), which is expected since the PEB is located closer to the planet. Even if the dispersion is very large, we may add that the influence of both the solar wind dynamic pressure and crustal magnetic field pressure

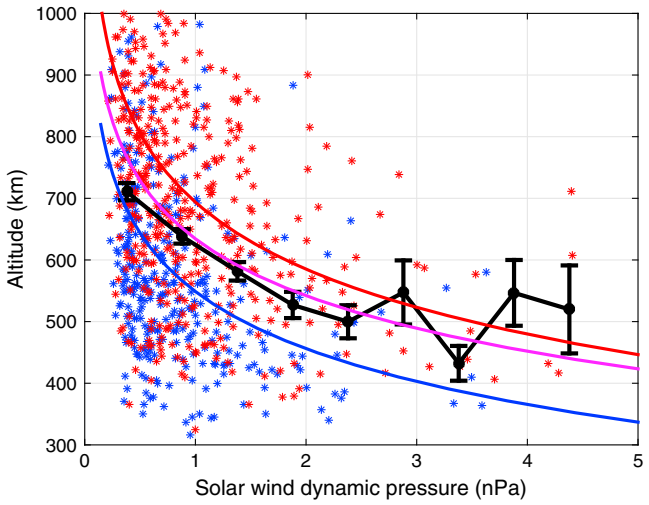

Figure 7. Estimated terminator altitude of the PEB crossings as a function of the solar wind dynamic pressure. The blue and red stars correspond, respectively, to weak and strong crustal field regions (based on the same definition as in Figure 6). The solid black line provides the median altitude (and standard deviation of the median) for 0.5 nPa bins. The magenta/blue/red solid lines give the best power law fits (see section 4.2 for further details) of all/weak crustal field/strong crustal field crossings.

are statistically very significant (assuming power laws), with Fisher tests (Box, 1953) providing risks—that is, probabilities that the influence is not real—of about 10^{-29} and 10^{-18}, respectively. These results are in agreement with a confinement of the atmosphere by the solar wind, which induces a draping of the IMF closer to the planet and thus pushes the PEB to lower altitudes, except when strong crustal fields locally act from below against this incident pressure.

4.2. Comparing the Parameters of Influence

Figure 8 shows the compared influence on the PEB terminator altitude of a number of parameters: extreme ultraviolet fluxes, solar zenith angle, local time, crustal magnetic field pressure, as well as solar wind dynamic pressure, density, velocity, and magnetic field. We shall mention that the EUV fluxes are derived from the FISM model (Chamberlin et al., 2007; available on the CDPP/AMDA database) at the 30.4 nm solar spectrum line which is the source of the 20–30 eV photoelectrons. Each set of parameters was then separated into low (below the median value of the parameter) and high (above the median value of the parameter) subsets of data to allow for a convenient comparison among the various parameters of influence. The median altitudes of the "low" and "high" subsets are then determined for each parameter. The standard deviation of the median value ($\frac{\sigma}{\sqrt{N}}$; σ standard deviation and N number of values) was shown in the figure instead of the classical standard deviation for a better visibility (σ is very large, about 200 km). We shall mention that in this figure we only considered the crossings for which all parameters were available (the solar wind parameters being available for only a part of them), which reduces the data set to 795 PEB crossings. However, the relative importance of the parameters is kept very similar if all crossings are considered for the EUV, LT, SZA, and crustal field parameters.

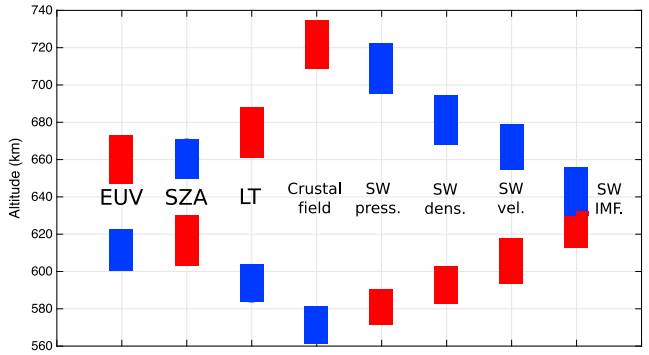

Figure 8. Compared influence of a number of parameters on the PEB terminator altitude: extreme ultraviolet (EUV) fluxes, solar zenith angle (SZA), local time (LT), crustal magnetic field, solar wind (SW), dynamic pressure (press.), density (dens.), velocity (vel.), and magnetic field (IMF). Each set of parameters was separated into low (below the median value of the parameter) and high (above the median value of the parameter) subsets of data. The median and standard deviation of the median are then calculated for the low and high subsets of each parameter, shown by rectangles in the figure (blue/red for the low/high subsets, with the height giving twice the standard deviation of the median). The rectangles of low/high subsets of the solar wind IMF cross each other, since the standard deviations overlap. The EUV fluxes are derived from the FISM model (Chamberlin et al., 2007; available on the CDPP/AMDA database) at the 30.4 nm solar spectrum line which is the source of the 20–30 eV photoelectrons; the crustal magnetic field pressure is calculated from the Morschhauser et al. (2014) model at a constant altitude of 400 km; the solar wind parameters are derived from the MAVEN SWIA and MAG data (Halekas et al., 2017).

The PEB terminator altitude thus increases with (by decreasing importance) increasing crustal magnetic field pressure, decreasing solar wind dynamic pressure, increasing local time, increasing EUV fluxes, and decreasing SZA and IMF. The two major parameters of influence are by far the solar wind dynamic and crustal magnetic field pressures, with a variation reaching 150 km of difference between the low and high median values.

More precisely, the low solar wind density seems even more efficient than a low velocity to cause an increase in the PEB altitude. Ramstad et al. (2015) showed that low solar wind densities lead to larger ion escape rates according to Mars Express ASPERA-3 data, since the atmosphere expands, giving more space and time for ionospheric plasma to accelerate, which leads to larger escape rates during the rarefaction (i.e., low SW density) events following the strong solar wind disturbances. We will discuss in section 5 how the solar wind dynamic pressure will impact the escape rates through the variable PEB altitude.

The influence of the other parameters—EUV, SZAm and LT—is less clear and depends on the frame considered (for the LT influence in MSO versus MSE) or on cross-correlations biases with the major drivers (for SZA near noon, as detailed above), even if the risks of artificial correlations as determined from Fisher's tests are always below 1%, except for the SZA influence (risk of ≈2%). Regarding the EUV influence, we point out that if EUV is a major driver for the photoelectron fluxes (Trantham et al., 2011; Xu et al., 2015) through the production mechanisms, its influence on the PEB should be less strong (e.g., the MGS data could not see any EUV influence

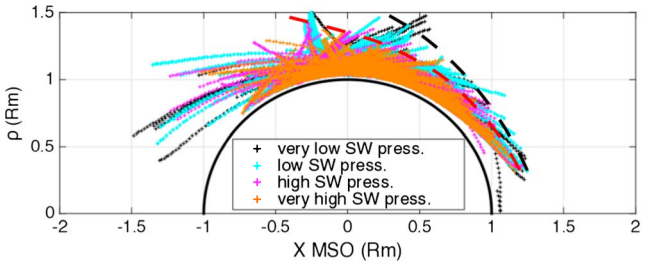

Figure 9. Influence of the solar wind dynamic pressure on the 20–30 eV photoelectron detection location in cylindrical MSO coordinates, assuming a continuous detection between inbound and outbound photoelectron line crossings and four levels of solar wind dynamic pressure conditions: very low corresponds to the P_{SW} <= 25% quantile, low to 25% < P_{SW} <= 50%, high to 50% < P_{SW} <= 75%, very high to P_{SW} > 75%. The two dashed lines represent sketched minimum and maximum altitude shapes for the photoelectron transport (see section 5 for more details).

on the ionopause, Mitchell et al., 2001). The EUV influence corresponds to an enhanced thermal pressure that will act against the solar wind confinement and thus push the draping of the IMF.

5. Discussion on the Photoelectron Escape

The PEB altitude is strongly influenced by the incident solar wind dynamic pressure that confines more or less the Martian ionosphere and that thus drives the location of the IMF draping around the planet. As shown in Figure 9 and explained below, the solar wind will consequently have a strong impact on the transport of the photoelectrons from the dayside to the tail region and eventually on the estimated escape rates derived.

In this figure, we assumed a continuous detection of 20–30 eV photoelectrons from the inbound to outbound crossings of the photoelectron line. This assumption is inaccurate in the nightside region, where a lot of electron depletions are observed, but it is mostly true otherwise, except at intermittent times in the noncollisional regions due to the strong plasma dynamics (mixing of several populations, accelerated particles, etc). We separated the time intervals into four categories, based on the value of the solar wind dynamic pressure at the times considered and superimposed the crossings on the figure in the following order: very low, low, high, and very high. The low and very low SW pressures are hidden behind the high and very high SW pressures close to the planet, but extend further than these. The photoelectron detection thus appears more and more confined close to the planet when higher solar wind dynamic pressure values are observed, not only on the dayside but also at terminator where the photoelectrons are on the way to escape down to the tail.

The PEB altitude is raised by low solar wind dynamic pressure conditions, leading to access to higher altitudes on the dayside for the photoelectrons, and thus transport along draped field lines toward the tail at higher altitudes as well. Overall, the photoelectron escape will not necessarily increase due to low solar wind dynamic pressure conditions, but the tail cross section to be considered for deriving escape rates increases. Frahm et al. (2010) provided the only known escape rates of photoelectrons ($3.14 \pm 1.78 \times 10^{23}$ electrons/s), and thus of corresponding ionospheric ions—assuming they escape at the same rate as the electrons, which may be overestimated if their large gyroradii make them impact the dense atmosphere—based on an average escape flux measured and a constant annular cross section of 1.16×10^{18} cm^2. This annular cross section was derived at $X = -1.5\,R_M$, with a minimum distance to the X axis of 2,850 km (no escaping photoelectrons at Mars were observed closer to the X axis) and an external limit at 6,700 km. However, our results show that the cross section to be considered for deriving escape rates is not a constant and will strongly depend on the PEB altitude on the dayside and thus, in particular, on the solar wind dynamic (and crustal magnetic field) pressure. Assuming sketched limits for low and high PEB altitudes (black and red lines in Figure 9), corresponding to about 200 km of difference near noon, and by extrapolating their shape to the tail until $X = -1.5\,R_M$, this will induce a variation of about 50% of the escape cross section. When escape rates are derived from single point in situ flux measurements, one should thus keep in mind that not only the measured local fluxes vary temporally and spatially but also the escape area (i.e., the cross section to be used) will significantly vary with time and depend on the dayside conditions. We mention that deriving MAVEN escape rates is beyond the scope of this paper, since it needs the quantitative analysis of the photoelectron peaks in the energy spectra (whereas we only focus on the PEB crossings here), but we plan to further investigate this in the future to analyze the variability of the escape rates during the MAVEN mission (with an average value that could be, or not, close to earlier estimates).

6. Characteristics Around the Boundary

Beyond the knowledge of the location and of the variability of the boundary, it is essential to better understand its nature and characteristics; therefore, we examine the evolution of a number of parameters around it. Figure 10 provides the average evolution of the 23–29 eV photoelectron integrated differential fluxes (Figure 10a), electron density (Figure 10c), electron differential fluxes at ~25 and ~130 eV (Figure 10c), as well as information on the pitch angle distributions (Figure 10b) and several magnetic field characteristics (Figures 10d–10f), as a function of the altitude around the boundary. The altitude 0 in the figure thus

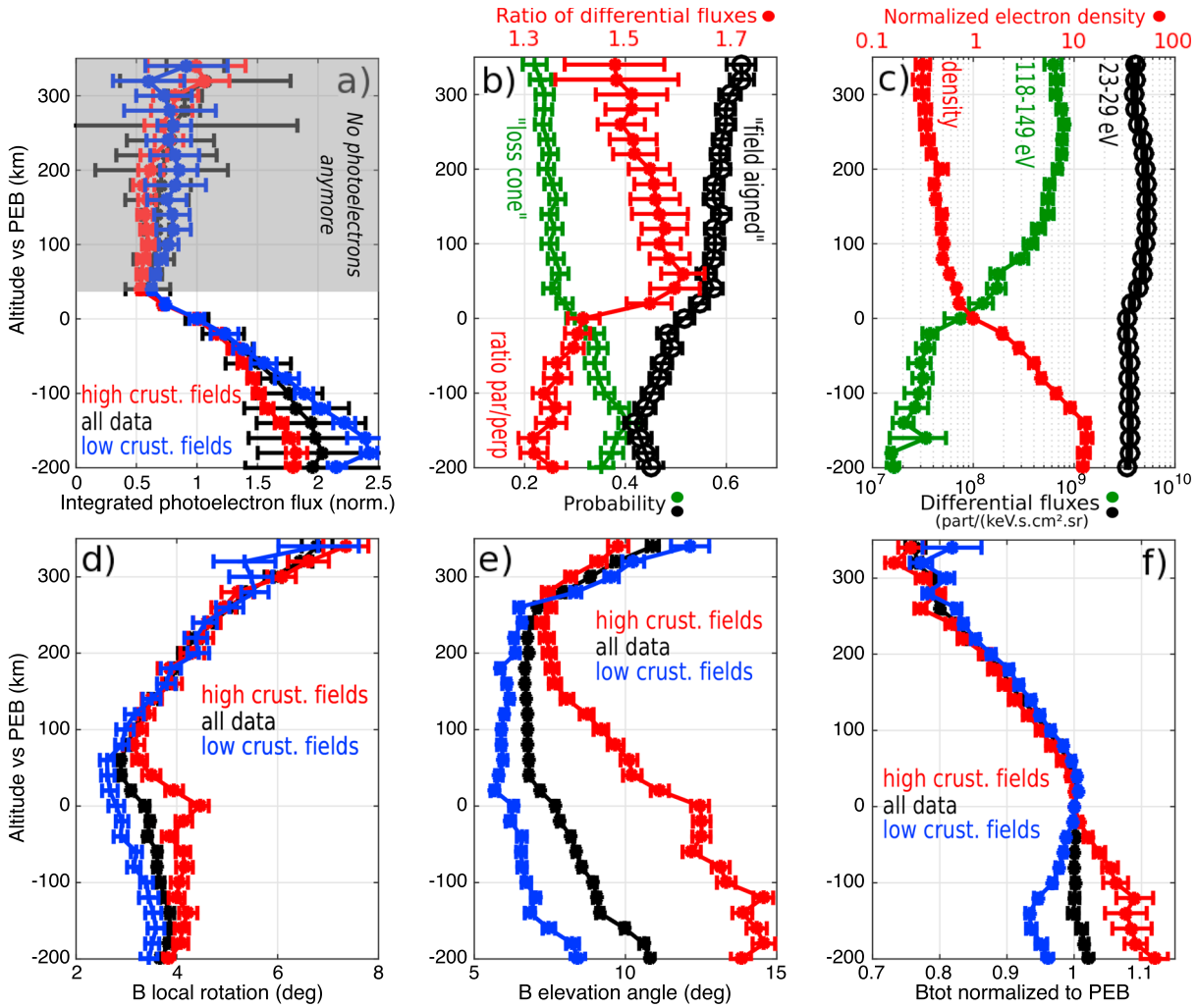

Figure 10. Average evolution of various parameters (eventually normalized, by the value at the PEB) as a function of altitude versus the PEB altitude (0 means the PEB altitude). (a) Normalized integrated 20–30 eV photoelectron flux from SWEA (shadowed part indicates incorrect photoelectron flux values); black/blue/red lines (as in Figures 10d–10f), respectively, correspond to all PEB crossings/only low crustal fields crossings/only high crustal fields crossings (see text). (b) Pitch angle information on 23–29 eV electrons: maximum ratio between parallel and perpendicular differential fluxes, probability of "loss cone" or "field-aligned" pitch angle distributions for the 0–90° range. (c) Mean SWEA differential fluxes of 23–29 eV and 118–149 eV electrons, and thermal electron density by LPW. (d) Local angular rotation, (e) elevation angle, and (f) normalized total magnitude of the in situ magnetic field measured by MAG. See text for more details.

corresponds to the altitude of each individual PEB crossing, while positive and negative values correspond respectively to altitudes above and below the crossing. Such a figure hides the various trajectories of the spacecraft, with, in particular, the altitude variation being different from one orbit to another, but it allows us to compare crossings occurring at different times and altitudes, by normalizing some of the parameters to avoid their strong temporal and/or spatial dynamics to hide the average characteristics of the PEB (e.g., for the electron density or total magnitude of the magnetic field).

We considered all MAVEN SWEA (with ~4 s time resolution) and MAG (with ~2 s time resolution) data at ±300 s around the time of each of the 1,696 PEB crossings available. Median (for Figures 10a, 10d, 10e, and 10f) or average (for Figures 10b and 10c) parameter values were then calculated for each 20 km altitude bin around the crossings, which leads to a maximum altitude range of 700 km. We however removed the data below −200 km since the average altitude actually increases below this limit, which would induce a bias for the interpretation if these data were kept. The standard deviation of the mean ($\frac{\sigma}{\sqrt{N}}$) is also shown for each parameter as an error bar. In Figures 10a, 10d, 10e, and 10f, we also considered three different profiles to identify the influence of the crustal fields: one, for all PEB crossings (black line) and two, for low (blue line) and high (red line) crustal field conditions at the crossings. These low/high conditions are determined by the 25th percentiles

of the crossings with the lowest and highest values of the Morschhauser et al. (2014) modeled crustal magnetic field values at 400 km altitude at the time of crossings.

Figure 10a provides the integrated 20–30 eV photoelectron flux, normalized by the flux at the time of each PEB crossing. Following the approach of Frahm et al. (2010), we integrated, for each time step, the photoelectron flux after removing the background spectrum (i.e., a power law fit) from 17.2 to 34.7 eV to extract the peak photoelectron fluxes only. Several tries were made with various energy ranges considered, leading to no significant qualitative change in the results, and the energy of the peak is very stable on the dayside. Above the PEB, the photoelectrons are by definition essentially absent, so that the fluxes should not be considered from about 50 km above the PEB (gray area), since they correspond to fluxes of magnetosheath electrons. The flux of upward moving photoelectrons gradually decreases when approaching the boundary, before a large drop in a ~100 km altitude shell centered on the PEB location, and ultimately, they disappear. We also find the presence of higher fluxes in the −200 to −100 km range when weak crustal fields are present, which may be related to an easier access of photoelectrons to altitudes above the photoelectron exobase (≈145–165 km altitude, see Xu, Liemohn, Bougher, et al., 2016) in the absence of strong horizontal closed crustal magnetic fields.

The median profiles of the magnetic field characteristics (local rotation every 4 s, Figure 10b; elevation angle, Figure 10c; magnitude of the field measured normalized by the value at the PEB) suggest the following average behavior from above to below the PEB. The magnetic field first drapes (and thus rotates less and less) and piles up (the total field increases) at altitudes above the PEB, which is consistent with the magnetic pileup region (MPR) characteristics, and is consistent with the fact that most data points considered here are located below the nominal magnetic pileup boundary location. The rotation of the field decreases toward lower altitudes, as does the magnetic field elevation angle that reaches a constant minimum value about 250 km above the PEB location. The situation seems, however, different with strong crustal fields: the interaction between upstream and crustal topologies induces on average an increase of the elevation angle ~150 km above the PEB (the influence of crustal fields may also be seen at the same time on the field rotation with a separation between low and high crustal field profiles). At 50 km above the PEB, while the photoelectron fluxes appear and strongly increase, the local rotation of the magnetic field increases slightly and reaches a peak exactly at the PEB in the presence of crustal fields (for this case the PEB marks a transition between two different configurations of the magnetic field, the draped field above and the crustal field below). We note that the absolute values of the rotation are small, which is due to the time resolution considered (4 s, a poorer resolution would lead to larger rotation angles). At the same time (i.e., 50 km or less above the PEB) the magnetic elevation angle slightly increases as well (all the more in the presence of crustal fields) and the total field keeps constant around the boundary (typical for the end of the MPR). Then, below the PEB, the rotation of the field stays small while the elevation angle slightly increases (with a more noisy behavior in the presence of crustal fields, due to the variable local topology) and the field magnitude decreases/increases in the absence/presence of crustal fields.

Figure 10b shows information regarding the pitch angle distribution of 23–29 eV electrons around the PEB (the most appropriate energy bin to investigate 20–30 eV photoelectrons with the pitch angle distribution (PAD) mode of the MAVEN SWEA instrument). The red line provides the ratio between the maximum parallel or antiparallel (maximum value among either the 0–45° or 135–180° pitch angle ranges) and perpendicular (45–135°) differential fluxes. The green and black lines give respectively the probability of "loss cone"and "field-*aligned" pitch angle distributions for the 0–90° range. We defined these categories based on an approach similar to Brain et al. (2007): each half of a PAD is taken separately (0–90° and 90–180°), and the standard deviation of fluxes of each half is calculated among the angular bins; the flux at 90° pitch angle is then compared to the most field-aligned flux for the spectrum (here at least <=30° or > =150° to avoid too narrow PADs); PAD spectra are separated according to whether the perpendicular flux at 90° exceeds the field-aligned flux by more than 1 standard deviation ("loss cone") or whether the field-aligned flux exceeds the perpendicular flux by more than 1 standard deviation ("field-aligned"). The rest of the spectra correspond to either isotropic or conic/anticonic spectra (not shown). We shall mention that only the qualitative behavior is discussed here, since changing the definition of the parameters modifies the absolute probabilities of each configuration.

Globally, the 23–29 eV electrons—that is, essentially photoelectrons below the PEB, magnetosheath electrons above it—PADs are more in a field-aligned configuration than in a loss cone configuration, except at

−140 km below the PEB, where both configurations have a similar probability. From about −200 km below the PEB until the boundary, the loss cone and field-aligned probabilities vary from, respectively, between 0.3 and 0.4 and between 0.4 and 0.5. The loss cone and field-aligned probabilities then abruptly decrease/increase from the PEB (or slightly below it) to about 50 km above it, before they keep stable at, respectively, ≈0.25 and ≈0.6 (with a slight continuous increase though). This change of PAD configuration at the PEB is clearly confirmed by the ratio between the maximum parallel (or antiparallel) and the perpendicular fluxes, which is roughly constant below and above the PEB but strongly increases from the PEB to 50 km above it (from 1.4 to 1.6), revealing an even more field-aligned configuration above than below the boundary (where the PADs are already more field aligned, with a ratio always above 1). As expected, the PADs are more in a field-aligned configuration (thus with more electrons on open field lines, at one end or both) than in a loss cone configuration (closed field lines). We are indeed looking at relatively high altitudes compared to the photoelectron exobase (Xu, Liemohn, Bougher, et al., 2016): 71/86% of the time steps considered correspond to altitudes above 300/400 km, respectively, with an average altitude reaching a minimum of 400 km (at about −150 km below the PEB, which explains the close green and black curves at this location). Moreover, plotting the probability of closed (loss cone + isotropic + conic PADs) and open (field-aligned + anticonic) fields configurations as a function of absolute altitude (not referenced to the PEB level; plot not shown) reveals an expected continuous decrease and increase versus altitude for these respective configurations, with equal probabilities at about 300–400 km. These observations are in agreement with the recent results by Xu et al. (2017) who investigated in details the low altitude topology and electron pitch angle distributions based on the shape parameter technique. This technique (see details in Xu et al., 2017) is based on a parameter whose value determines the nature of the electron spectra (photoelectrons or solar wind) after a comparison between measured spectra and a ionosphere reference spectrum (that includes the 20–30 eV peaks and the sharp drop at 60–70 eV). The authors showed that closed field lines are mostly observed at low altitudes (and above crustal fields), and that above 400 km altitudes the field lines are mostly open and draped around the planet.

Figure 10c shows the mean absolute differential fluxes of 23–29 eV (black lines) and 118–149 eV (green lines) electrons around the PEB, the low energy range corresponding to either photoelectrons (mostly below the PEB) or magnetosheath electrons (mostly above the PEB), while the high energy range corresponds essentially to magnetosheath electrons only and keeps a good signal-to-noise ratio compared to higher energy ranges. The PEB appears as a clear transition between the photoelectron-dominated and magnetosheath electron-dominated regions, with magnetosheath electron fluxes dropping above the PEB (by up to 1 order of magnitude in about 50–100 km for the highest energies), while the photoelectrons fluxes (i.e., 23–29 eV electrons below the PEB) appear and increase below the boundary (since the photoelectron source region is at low altitudes). We shall mention that the profiles are similar for all crustal field conditions. Meanwhile, a strong change in the density profile occurs at the PEB altitude, with a clear and large increase of the gradient with altitude from above to below the PEB. Moreover, one can note that plotting the absolute densities (not normalized to 1 at the PEB; not shown) as a function of altitude versus the PEB confirms our conclusions with the same strong change of slope above the PEB. Finally, in addition to this observation of smaller density gradients above the PEB (and not larger gradients as may be used to define the ionopause), the 1000 cm^{-3} density level used by Han et al. (2014) to define the ionopause level is located in our data set at ∼440 km, which is similar to the Mars Express results (and ∼200 km below our average PEB altitude): these results thus confirm that the PEB and ionopause (as defined by large density gradients or the 1,000 cm^{-3} density level) are not located at the same altitude on average. We shall mention that the normalization of both the density and altitude axes of Figure 10c make it impossible to add the location of the ionopause on the same figure even as defined from a constant density level.

The average variability of plasma and magnetic fields around the PEB altitude thus reveals several characteristics:

1. The 20–30 eV photoelectron flux first gradually decreases from below the PEB, followed by a strong decrease around the PEB over an altitude shell "thickness" of the order of 100 km altitude until photoelectrons disappear.
2. The magnetic field is characteristic for the magnetic pileup region above the PEB, with a strong (decreasing toward the PEB) rotation of the field and a decreasing elevation until the field gets draped; the field magnitude increases linearly until it gets stable around the PEB, where a local increase of rotation and elevation is observed; finally, the crustal fields determine the low-altitude topology (and influence the topology at least until 150 km above the PEB).

3. The pitch angle distributions of 23–29 eV electrons (i.e., photoelectrons below the PEB) show a steep increase of the ratio between parallel (or antiparallel, the maximum value being considered) and perpendicular fluxes at the PEB, and an increase/decrease of the probability for field-aligned/loss cone PADs at the same time, even if the PADs reveal more open field lines than closed field lines at the altitudes considered in our study (in agreement with Xu et al., 2017).
4. The electron fluxes reveal a steep increase of high-energy electrons (i.e., magnetosheath type electrons) above the PEB and a smaller decrease of 25 eV electron fluxes, while the slope of the density profile strongly increases at the PEB; the PEB is thus on average different from an ionopause defined by either a stronger density depletion or by a 1,000 cm^{-3} density level (Han et al., 2014) (which actually also occurs about 200 km below the PEB on the MAVEN data). The PEB thus appears as a flux and density transition region between ionospheric and magnetosheath electrons.

Overall, these characteristics are consistent with the classical picture of the PEB as the location where photoelectrons, after their upward transport above the exobase (modified by the magnetic topology, in particular, crustal fields), encounter open draped field lines, with more field-aligned PADs and get convected toward the tail and eventually escape. However, beyond the coherent average profiles discussed in this section, a large dispersion appears when individual crossings are analyzed. The dispersion (ratio between standard deviation and mean values) is most often above one for all particles parameters (photoelectron flux, electron fluxes and density, and pitch angle profiles) and at all altitudes. The small error bars of Figure 10 actually correspond to the standard deviation of the mean (i.e., much smaller than the nominal standard deviation). In the future, individual crossings will be investigated in more details to better understand the large dynamics beyond the global trends discussed above.

7. Conclusions

The characterization of the plasma boundaries at Mars and their difference has been a matter of debate for many years. In particular, the photoelectron boundary (PEB) discovered by Mars Global Surveyor and defined by the disappearance of ionospheric photoelectrons, still remains poorly understood. We provide in this paper a detailed description of the PEB based on a manual detection of almost 1,700 boundary crossings from MAVEN data before May 2016. We thus determined its shape, its parameters of influence, the variability of several parameters (magnetic field, photoelectron fluxes, etc.) in the vicinity of the boundary, and its influence on the plasma escape fluxes. Our main conclusions are the following.

1. First, the PEB appears approximately as a circular boundary ($e = 0.0047$) with a highly variable altitude that is strongly related to the draping of the IMF around the planet, and mostly depends on the solar wind dynamic and crustal magnetic field pressures (more than extreme ultraviolet fluxes or solar zenith angle and local time). These pressures will push from above (for the solar wind) or below (for the crustal fields) the draping magnetic field topology and thus modify the location where the upward moving photoelectrons will encounter the draped open field lines to get eventually convected toward the tail.
2. Second, we show how the variable PEB altitude on the dayside, due to several drivers, will allow the access of photoelectrons to variable altitudes toward the terminator and thus affect their transport along draped field lines toward the tail and strongly modify (up to ~50%) the tail cross section to be considered for deriving escape rates of photoelectrons (and associated ions assuming neutrality). When escape rates are derived from single-point in situ flux measurements, the temporal and spatial variations of the dayside PEB altitude will thus determine the escape cross section to be considered.
3. Finally, the detailed analysis of plasma and magnetic field characteristics around the PEB crossings shows that the boundary is not always sharp and is characterized on average by the following:
    a. a gradual decrease of the photoelectron flux much before the PEB and a more steep decrease around it over an altitude "thickness" of the order of 100 km;
    b. a magnetic field topology typical for the end of the magnetic pileup region above it, with also a locally increased rotation and elevation angle of the field at the PEB, all the more in the presence of crustal field sources;
    c. more field-aligned fluxes above than below the boundary, despite a more "open" than "closed" field configuration usually much below the PEB; and
    d. a clear change of altitude slopes for both the electron fluxes (in particular, for high-energy electrons) and total density; the density slope indeed decreases from below to above the boundary, the PEB

being thus different from the ionopause if defined by a stronger density slope, and more precisely located ~200 km below the PEB if defined as the 1,000 cm^{-3} density level.

However, beyond these average characteristics of the PEB, a large dispersion appears when individual crossings are analyzed and should be investigated in the future. Furthermore, a more detailed understanding of the various plasma boundaries (MPB/IMB, pressure boundary, ion composition boundary, ionopause, etc.) and of the physical processes linking them will need future common work, by taking advantage of the complete particles and fields package of the MAVEN mission.

Acknowledgments
This work was supported by the French space agency CNES for the observations obtained with the SWEA instrument embarked on MAVEN. The authors acknowledge the support of the MAVEN instrument and science teams, as well as the CDPP/AMDA team (http://amda.cdpp.eu) and Emmanuel Penou for providing support with data analysis tools. The MAVEN data are taken from the Berkeley database with the "spdsoft" software.

References

Barabash, S., Lundin, R., Andersson, H., Brinkfeldt, K., Grigoriev, A., Gunell, H., … Thocaven, J.-J. (2006). The Analyzer of Space Plasmas and Energetic Atoms (ASPERA-3) for the Mars Express mission. *Space Science Reviews*, *126*(1), 113–164. https://doi.org/10.1007/s11214-006-9124-8

Bertucci, C., Mazelle, C., Crider, D. H., Mitchell, D. L., Sauer, K., Acuña, M. H., … Winterhalter, D. (2004). MGS MAG/ER observations at the magnetic pileup boundary of Mars: Draping enhancement and low frequency waves. *Advances in Space Research*, *33*, 1938–1944. https://doi.org/10.1016/j.asr.2003.04.054

Box, G. (1953). Non-normality and tests on variances. *Biometrika*, *40*(3–4), 318–335. https://doi.org/10.1093/ biomet/40.3-4.318

Brain, D. A., Barabash, S., Bougher, S. W., Duru, F., Jakosky, B. M., & Modolo, R. (2017). *Solar Wind Interaction and Atmospheric Escape* (pp. 433–463). Cambridge: Cambridge Planetary Science, Cambridge University Press. https://doi.org/10.1017/9781139060172.015

Brain, D. A., Lillis, R. J., Mitchell, D. L., Halekas, J. S., & Lin, R. P. (2007). Electron pitch angle distributions as indicators of magnetic field topology near Mars. *Journal of Geophysical Research*, *112*, A09201. https://doi.org/10.1029/2007JA012435

Carlsson, E., Brain, D., Luhmann, J., Barabash, S., Grigoriev, A., Nilsson, H., & Lundin, R. (2008). Influence of IMF draping direction and crustal magnetic field location on Martian ion beams. *Planetary and Space Science*, *56*(6), 861–867. https://doi.org/10.1016/j.pss.2007.12.016

Chamberlin, P. C., Woods, T. N., & Eparvier, F. G. (2007). Flare Irradiance Spectral Model (FISM): Daily component algorithms and results. *Space Weather*, *5*, S07005. https://doi.org/10.1029/2007SW000316

Coates, A. J., Tsang, S. M. E., Wellbrock, A., Frahm, R. A., Winningham, J. D., Barabash, S., … Crary, F. J. (2011). Ionospheric photoelectrons: Comparing Venus, Earth, Mars and Titan. *Planetary and Space Science*, *59*, 1019–1027. https://doi.org/10.1016/j.pss.2010.07.016

Coates, A. J., Wellbrock, A., Frahm, R. A., Winningham, J. D., Fedorov, A., Barabash, S., & Lundin, R. (2015). Distant ionospheric photoelectron energy peak observations at Venus. *Planetary and Space Science*, *113*, 378–384. https://doi.org/10.1016/j.pss.2015.02.003

Connerney, J. E. P., Espley, J., Lawton, P., Murphy, S., Odom, J., Oliversen, R., & Sheppard, D. (2015). The MAVEN magnetic field investigation. *Space Science Reviews*, *195*, 257–291. https://doi.org/10.1007/s11214-015-0169-4

Crider, D. H., Vignes, D., Krymskii, A. M., Breus, T. K., Ness, N. F., Mitchell, D. L., … Acuña, M. H. (2003). A proxy for determining solar wind dynamic pressure at Mars using Mars Global Surveyor data. *Journal of Geophysical Research*, *108*, 1461. https://doi.org/10.1029/2003JA009875

Dubinin, E., Fränz, M., Woch, J., Roussos, E., Barabash, S., Lundin, R., … Acuña, M. (2006). Plasma morphology at Mars. Aspera-3 observations. *Space Science Reviews*, *126*, 209–238. https://doi.org/10.1007/s11214-006-9039-4

Edberg, N. J. T., Lester, M., Cowley, S. W. H., & Eriksson, A. I. (2008). Statistical analysis of the location of the Martian magnetic pileup boundary and bow shock and the influence of crustal magnetic fields. *Journal of Geophysical Research*, *113*, A08206. https://doi.org/10.1029/2008JA013096

Frahm, R. A., Sharber, J. R., Winningham, J. D., Link, R., Liemohn, M. W., Kozyra, J. U., … Fedorov, A. (2010). Estimation of the escape of photoelectrons from Mars in 2004 liberated by the ionization of carbon dioxide and atomic oxygen. *Icarus*, *206*, 50–63. https://doi.org/10.1016/j.icarus.2009.03.024

Frahm, R. A., Sharber, J. R., Winningham, J. D., Wurz, P., Liemohn, M. W., Kallio, E., … McKenna-Lawler, S. (2006). Locations of atmospheric photoelectron energy peaks within the Mars environment, *126*, 389–402. https://doi.org/10.1007/s11214-006-9119-5

Halekas, J. S., Ruhunusiri, S., Harada, Y., Collinson, G., Mitchell, D. L., Mazelle, C., … Jakosky, B. M. (2017). Structure, dynamics, and seasonal variability of the Mars-solar wind interaction: MAVEN solar wind ion analyzer in-flight performance and science results. *Journal of Geophysical Research: Space Physics*, *122*, 547–578. https://doi.org/10.1002/2016JA023167

Han, X., Fraenz, M., Dubinin, E., Wei, Y., Andrews, D. J., Wan, W., … Barabash, S. (2014). Discrepancy between ionopause and photoelectron boundary determined from Mars Express measurements. *Geophysical Research Letters*, *41*, 8221–8227. https://doi.org/10.1002/2014GL062287

Jakosky, B. M., Lin, R. P., Grebowsky, J. M., Luhmann, J. G., Mitchell, D. F., Beutelschies, G., … Zurek, R. (2015). The Mars Atmosphere and Volatile EvolutioN (MAVEN) mission. *Space Science Reviews*, *195*, 3–48. https://doi.org/10.1007/s11214-015-0139-x

Liemohn, M. W., Frahm, R. A., Winningham, J. D., Ma, Y., Barabash, S., Lundin, R., … Dierker, C. (2006). Numerical interpretation of high-altitude photoelectron observations. *Icarus*, *182*, 383–395. https://doi.org/10.1016/j.icarus.2005.10.036

Lundin, R., Barabash, S., Andersson, H., Holmström, M., Grigoriev, A., Yamauchi, M., … Bochsler, P. (2004). Solar wind-induced atmospheric erosion at Mars: First results from ASPERA-3 on Mars Express. *Science*, *305*(5692), 1933–1936. https://doi.org/10.1126/science.1101860

Mantas, G. P., & Hanson, W. B. (1979). Photoelectron fluxes in the Martian ionosphere. *Journal of Geophysical Research*, *84*, 369–385. https://doi.org/10.1029/JA084iA02p00369

Matsunaga, K., Seki, K., Brain, D. A., Hara, T., Masunaga, K., McFadden, J. P., … Jakosky, B. M. (2015). Comparison of Martian magnetic pileup boundary with ion composition boundary observed by MAVEN. *American Geophysical Union, Fall Meeting 2015, Abstract P21A-2071*.

Mitchell, D. L., Lin, R. P., Mazelle, C., Rème, H., Cloutier, P. A., Connerney, J. E. P., … Ness, N. F. (2001). Probing Mars' crustal magnetic field and ionosphere with the MGS electron reflectometer. *Journal of Geophysical Research*, *106*, 23,419–23,428. https://doi.org/10.1029/2000JE001435

Mitchell, D. L., Lin, R. P., Rème, H., Crider, D. H., Cloutier, P. A, Connerney, J. E. P., … Ness, N. F (2000). Oxygen auger electrons observed in Mars' ionosphere. *Geophysical Research Letters*, *27*, 1871–1874. https://doi.org/10.1029/1999GL010754

Mitchell, D. L., Mazelle, C., Sauvaud, J.-A., Thocaven, J.-J., Rouzaud, J., Fedorov, A., … Jakosky, B. M. (2016). The MAVEN solar wind electron analyzer. *Space Science Reviews*, *200*, 495–528. https://doi.org/10.1007/s11214-015-0232-1

Morschhauser, A., Lesur, V., & Grott, M. (2014). A spherical harmonic model of the lithospheric magnetic field of Mars. *Journal of Geophysical Research: Planets*, *119*, 1162–1188. https://doi.org/10.1002/2013JE004555

Nagy, A. F, wINTerhalter, D., Sauer, K., Cravens, T. E, Brecht, S., Mazelle, C., … Trotignon, J. G (2004). The plasma environment of Mars. *Space Science Reviews*, *111*, 33–114. https://doi.org/10.1023/B: SPAC.0000032718.47512.92

Ramstad, R., Barabash, S., Futaana, Y., Nilsson, H., Wang, X.-D., & Holmström, M. (2015). The Martian atmospheric ion escape rate dependence on solar wind and solar EUV conditions: 1. Seven years of Mars Express observations. *Journal of Geophysical Research: Planets*, *120*, 1298–1309. https://doi.org/10.1002/2015JE004816

Riedler, W., Schwingenschuh, K., Moehlmann, D., Oraevskii, V. N, Eroshenko, E., & Slavin, J. (1989). Magnetic fields near Mars—First results. *Nature*, *341*, 604–607. https://doi.org/10.1038/341604a0

Rosenbauer, H., Shutte, N., Galeev, A., Gringauz, K., & Apathy, I. (1989). Ions of Martian origin and plasma sheet in the Martian magnetosphere—Initial results of the TAUS experiment. *Nature*, *341*, 612–614. https://doi.org/10.1038/341612a0

Sakai, S., Rahmati, A., Mitchell, D. L., Cravens, T. E., Bougher, S. W., Mazelle, C., … Jakosky, B. M. (2015). Model insights into energetic photoelectrons measured at Mars by MAVEN. *Geophysical Research Letters*, *42*, 8894–8900. https://doi.org/10.1002/2015GL065169

Steckiewicz, M., Garnier, P., André, N., Mitchell, D. L., Andersson, L., Penou, E., … Jakosky, B. M. (2017). Comparative study of the Martian suprathermal electron depletions based on Mars Global Surveyor, Mars Express, and Mars atmosphere and volatile evolution mission observations. *Journal of Geophysical Research: Space Physics*, *122*, 857–873. https://doi.org/10.1002/2016JA023205

Steckiewicz, M., Mazelle, C., Garnier, P., André, N., Penou, E., Beth, A., … Jakosky, B. M. (2015). Altitude dependence of nightside Martian suprathermal electron depletions as revealed by MAVEN observations. *Geophysical Research Letters*, *42*, 8877–8884. https://doi.org/10.1002/2015GL065257

Trantham, M., Liemohn, M., Mitchell, D., & Frank, J. (2011). Photoelectrons on closed crustal field lines at Mars. *Journal of Geophysical Research*, *116*, A07311. https://doi.org/10.1029/2010JA016231

Trotignon, J. G., Mazelle, C., Bertucci, C., & Acuña, M. H. (2006). Martian shock and magnetic pile-up boundary positions and shapes determined from the Phobos 2 and Mars Global Surveyor data sets. *Planetary and Space Science*, *54*, 357–369. https://doi.org/10.1016/j.pss.2006.01.003

Tsang, S. M. E., Coates, A. J., Jones, G. H., Frahm, R. A., Winningham, J. D., Barabash, S., … Fedorov, A. (2015). Ionospheric photoelectrons at Venus: Case studies and first observation in the tail. *Planetary and Space Science*, *113*, 385–394. https://doi.org/10.1016/j.pss.2015.01.019

Vignes, D., Acuña, M. H., Connerney, J. E. P., Crider, D. H., Reme, H., & Mazelle, C. (2002). Factors controlling the location of the bow shock at Mars. *Geophysical Research Letters*, *29*(9), 42–1–42–4. https://doi.org/10.1029/2001GL014513

Wellbrock, A., Coates, A. J., Sillanpää, I., Jones, G. H., Arridge, C. S., Lewis, G. R., … Aylward, A. D. (2012). Cassini observations of ionospheric photoelectrons at large distances from Titan: Implications for Titan's exospheric environment and magnetic tail. *Journal of Geophysical Research*, *117*, A03216. https://doi.org/10.1029/2011JA017113

Xu, S., Liemohn, M., Bougher, S., & Mitchell, D. (2015). Enhanced carbon dioxide causing the dust storm-related increase in high-altitude photoelectron fluxes at Mars. *Geophysical Research Letters*, *42*, 9702–9710. https://doi.org/10.1002/2015GL066043

Xu, S., Mitchell, D., Liemohn, M., Dong, C., Bougher, S., Fillingim, M., … Jakosky, B. (2016). Deep nightside photoelectron observations by MAVEN SWEA: Implications for Martian northern hemispheric magnetic topology and nightside ionosphere source. *Geophysical Research Letters*, *43*, 8876–8884. https://doi.org/10.1002/2016GL070527

Xu, S., Liemohn, M., Bougher, S., & Mitchell, D. (2016). Martian high-altitude photoelectrons independent of solar zenith angle. *Journal of Geophysical Research: Space Physics*, *121*, 3767–3780. https://doi.org/10.1002/2015JA022149

Xu, S., Liemohn, M. W., Dong, C., Mitchell, D. L., Bougher, S. W., & Ma, Y. (2016). Pressure and ion composition boundaries at Mars. *Journal of Geophysical Research: Space Physics*, *121*, 6417–6429. https://doi.org/10.1002/2016JA022644

Xu, S., Mitchell, D., Liemohn, M., Fang, X., Ma, Y., Luhmann, J., … Jakosky, B. (2017). Martian low-altitude magnetic topology deduced from MAVEN/SWEA observations. *Journal of Geophysical Research: Space Physics*, *122*, 1831–1852. https://doi.org/10.1002/2016JA023467